Differential dynamic microscopy of weakly scattering and polydisperse protein-rich clusters

Mohammad S. Safari,[1] Maria A. Vorontsova,[1] Ryan Poling-Skutvik,[1] Peter G. Vekilov,[1,2,*] and Jacinta C. Conrad[1,†]
[1]*Department of Chemical and Biomolecular Engineering, University of Houston, Houston, Texas 77204-4004, USA*
[2]*Department of Chemistry, University of Houston, Houston, Texas 77204-4004, USA*
(Received 29 January 2015; revised manuscript received 5 October 2015; published 23 October 2015)

Nanoparticle dynamics impact a wide range of biological transport processes and applications in nanomedicine and natural resource engineering. Differential dynamic microscopy (DDM) was recently developed to quantify the dynamics of submicron particles in solutions from fluctuations of intensity in optical micrographs. Differential dynamic microscopy is well established for monodisperse particle populations, but has not been applied to solutions containing weakly scattering polydisperse biological nanoparticles. Here we use bright-field DDM (BDDM) to measure the dynamics of protein-rich liquid clusters, whose size ranges from tens to hundreds of nanometers and whose total volume fraction is less than 10^{-5}. With solutions of two proteins, hemoglobin A and lysozyme, we evaluate the cluster diffusion coefficients from the dependence of the diffusive relaxation time on the scattering wave vector. We establish that for weakly scattering populations, an optimal thickness of the sample chamber exists at which the BDDM signal is maximized at the smallest sample volume. The average cluster diffusion coefficient measured using BDDM is consistently lower than that obtained from dynamic light scattering at a scattering angle of 90°. This apparent discrepancy is due to Mie scattering from the polydisperse cluster population, in which larger clusters preferentially scatter more light in the forward direction.

DOI: 10.1103/PhysRevE.92.042712 PACS number(s): 87.15.Vv, 87.64.M−, 82.70.−y, 87.14.E−

I. INTRODUCTION

Diffusive dynamics play an important role in many biological transport processes, including intracellular transport [1–3], bacterial motility [4], biofilm growth [5], and protein aggregation, complexation, and crystallization [6–8], and additionally may affect the efficacy of emerging nanomedicine-based therapies [9–12]. Understanding the role of dynamics in both natural and engineered processes requires methods to quantify the motion of micro- and nanoscale particles in complex biological media. Traditionally, scattering methods such as dynamic light scattering (DLS) [13] have been used to measure the dynamics of submicron particles. Measurements of biological dynamics in complex media *in vitro* or *in vivo*, however, may be incompatible with DLS, which requires optically transparent samples and low concentrations of scatterers. In addition, many biological particles, including bacteria, protein complexes, polyplexes, viruses, and cellular organelles, scatter light only weakly. Optical microscopy coupled with particle-tracking techniques [14] circumvents some of the limitations inherent to scattering methods and hence is widely employed to measure microscale particle dynamics in biological settings. Biological particles, however, may be smaller than the resolution limit of an optical microscope (∼400 nm), precluding the use of standard bright-field microscopy. Fluorescence labeling of biological particles [15] and/or superresolution optical microscopy techniques [16] can allow access to the dynamics of particles smaller than the optical resolution limit, yet these methods also exhibit disadvantages for dynamic measurements: Fluorescent labels may perturb biological function and the acquisition times required for many superresolution methods may be too long to access the fast dynamics of submicron particles. There remains an unmet need for simple and nonperturbing methods to measure dynamics of nanoscale biological objects in complex media.

Differential dynamic microscopy (DDM) is a recently developed variant of digital Fourier microscopy [17] that yields measurements of the dynamics of submicron particles [18]. In DDM, the dynamics of particles in solution are obtained by analyzing the Fourier spectrum of a time series of difference images [19]. The resulting function describes the decorrelation of intensity fluctuations and contains the intermediate scattering function measured in DLS [19]. Differential dynamic microscopy has two key advantages: First, it yields measurements of the dynamics of particles whose size is smaller than the optical resolution limit [18,19]; second, its simplest implementation requires only a standard optical microscope, incoherent (white light) illumination, and a digital video camera, although extensions to fluorescence [19] and confocal [20] microscopy add specificity and resolution. As a result, this method has been used to characterize the dynamics of monodisperse spherical [21] and anisotropic [22–24] nanoparticles and bacteria [25–27] in complex geometries [28,29]. Despite these achievements, two factors currently limit the use of DDM for nanoscale biological particles. First, how to generate sufficient DDM signal from weakly scattering biological systems while maintaining low sample volumes has not been addressed. Second, how dispersity in the particle size affects the dynamics measured in DDM remains poorly understood. A fundamental understanding of the effects of weak scattering and size polydispersity on DDM signal generation will allow this method to be applied to characterize the dynamics of a wide range of biological particles.

Here we demonstrate the applicability of bright-field DDM (BDDM) to characterize weakly scattering and polydisperse biological nanoscale objects. As model systems we use undersaturated solutions of two proteins, hemoglobin A and lysozyme, that contain polydisperse protein-rich liquid clusters of radius 70–250 nm [30–38]. Hemoglobin A is

*vekilov@uh.edu
†jcconrad@uh.edu

the main oxygen-transporting protein found in red blood cells; the presence of free heme in solution (the prosthetic group of hemoglobin) promotes the formation of hemoglobin clusters [39]. Lysozyme is a well-studied and robust protein for which cluster formation is thought to be due to conformational changes in the lysozyme dimer [40]. Both solutions scatter light only weakly and the properties of the clusters of both proteins remain constant over many hours at room temperature. Using BDDM, we obtain the average diffusion coefficient from the wave-vector dependence of the diffusive relaxation time. First, we show that the signal-to-noise ratio obtained in BDDM depends on the thickness of the sample chamber; as a consequence, the accessible range of wave vectors is maximized with minimal sample volume at an optimal chamber thickness. Second, we find that the average diffusion coefficient of clusters obtained from BDDM measurements is consistently smaller than that obtained from DLS at a scattering angle of 90°. We attribute the apparent discrepancy between BDDM and DLS to a combination of Mie scattering and polydispersity: BDDM accesses smaller scattering angles than DLS and hence captures more signal from the larger clusters, which preferentially scatter more light in the forward direction. These results demonstrate that DDM is a simple yet powerful tool for characterizing weakly scattering and polydisperse submicron particles, including many found in biological settings.

II. METHODS

A. Reagents and solutions

Lyophilized lysozyme, purchased from Affymetrix, was dissolved at ∼200 mg ml^{-1} in pure deionized (DI) water. Protein concentration was determined by absorbance measurements using a Beckman Coulter DU 800 spectrophotometer and extinction coefficient $\epsilon = 2.64$ ml mg^{-1} cm^{-1} at 280 nm. The solution was dialyzed for two days against DI water to remove undesired low molecular weight salts. After dialysis, the solution was adjusted to a concentration of 103 mg ml^{-1} and filtered through 0.45-μm Polyethersulfone (PES) syringe filters prior to all measurements. The measured pH of this solution was 5.41, likely due to acidic salts present in the lyophilized powder after purification.

Normal adult hemoglobin (hemoglobin A) was obtained by lysis of red blood cells obtained from a healthy donor following institutional and NIH regulations; for details of this procedure, see Ref. [41]. It was purified by ion-exchange chromatography and stored in liquid nitrogen. A solution sample was thawed and diluted to 50 mg ml^{-1} in potassium phosphate buffer at a concentration of 0.15M and pH 7.35. The hemoglobin A concentration was determined using Drabkin's reagent (which converts hemoglobin to the cyan-met form) and extinction coefficient $\epsilon = 0.6614$ ml mg^{-1} cm^{-1} at 540 nm for cyan-met hemoglobin. The solution was filtered through 0.22-μm PES syringe filters prior to all measurements.

B. Differential dynamic microscopy

Samples for differential dynamic microscopy were sealed in glass chambers constructed from cover glasses. Two (22 × 22)-mm^2 cover glasses (thickness 0.19–0.23 mm, Fisherbrand), separated laterally by ∼10 mm, were attached to a rectangular cover glass with dimensions of 48 × 65 mm^2 (thickness 0.13–0.17 mm, Gold Seal) using an epoxy-based adhesive (Devcon). A (22 × 22)-mm^2 cover glass was then centered on top of the two cover glasses to create an open chamber. One side of the chamber was sealed with epoxy. Protein solution was introduced into the chamber through the open side, which was then closed with epoxy [21]. We assumed that the thickness of this chamber was 160 μm.

To study the effects of chamber thickness on the BDDM signal, we also used borosilicate square capillaries (Vitrocom) with internal diameters of 500 and 800 μm. To access thicknesses smaller than 160 μm, we designed a wedge-shaped chamber. In this case, a single (22 × 22)-mm^2 cover glass (thickness 0.19–0.23 mm, Fisherbrand) was attached using a UV adhesive (Norland Adhesive) to a rectangular cover glass with dimensions 48 × 65 mm^2 (thickness 0.13–0.17 mm, Gold Seal). A (22 × 22)-mm^2 cover glass was placed over the top to create an open wedge-shaped chamber. One of the open sides was sealed completely using UV adhesive; the other one was partially sealed. Protein solution was introduced from the half-open side, which was subsequently sealed with UV adhesive.

To calibrate the thickness at different locations along the wedge-shaped chamber, we filled it with a solution of fluorescently labeled poly(methyl methacrylate) (PMMA) particles. The chamber was imaged with a confocal point scanner (VT-Eye, VisiTech International) attached to an inverted microscope (Leica DM4000) with a 100× oil-immersion objective (Leica Microsystems HCX PL APO, numerical aperture of 1.4) at a wavelength of 491 nm. The thickness at a select location was evaluated as the difference between the highest and lowest microscope stage positions at which fluorescently labeled PMMA particles were in focus. This method was constrained to thicknesses lower than 80 μm. To determine higher thicknesses in the same chamber, up to 125 μm, we assumed that the increase in thickness was linear and extrapolated from the measured thicknesses using the distance from the thin chamber edge.

For BDDM data collection, protein solutions were imaged on a Leica inverted microscope attached to an 100× oil-immersion objective using a high-speed 8-bit AOS camera (AOS Technologies AG). The microscope was equipped with a condenser of numerical aperture 0.7; an electronic aperture inside the microscope was partly closed during measurements, reducing the effective numerical aperture to approximately 0.41 for hemoglobin and approximately 0.23 for lysozyme and introducing maximum angles $\theta_{\max}$ of 24.5° and 14°, respectively. We recorded multiple series of 4200 images of size 480 × 640 pixels^2 at a frame rate of 63 frames per second. To extract the dynamics of cluster diffusion from micrographs, a DDM algorithm was implemented as described in Ref. [21]. Images separated by a fixed lag time τ were subtracted to obtain the intensity difference $\Delta(x,y;\tau) = I(x,y;t+\tau) - I(x,y;t)$, where $I(x,y;t)$ was the intensity at position (x,y) measured at time t. Here τ ranged from 0.0158 to 25 s. Because the size of clusters fell below the resolution limit of microscope, image subtraction generated a speckle pattern. We computed the two-dimensional Fourier transform of $\Delta(x,y;\tau)$ and averaged over all image pairs

with the same τ. This procedure yielded a Fourier power spectrum $\Delta(u_x,u_y;\tau)$, where u_x and u_y were the coordinates in Fourier space. For a given τ, averaging was performed over $4200 - n_f$ image pairs, where $n_f = \mathcal{F}\tau$, with $\mathcal{F}$ denoting the frame rate. The Brownian motion of clusters was not geometrically constrained and as a result the two-dimensional (2D) power spectra were isotropic. We therefore averaged the 2D power spectra azimuthally to obtain image structure functions $\Delta(q,\tau)$, where $q = 2\pi\sqrt{u_x^2+u_y^2}$ is the wave-vector magnitude.

The light scattered by monomers at small angles was negligible and hence the BDDM signal was predominantly due to cluster diffusion. In the DDM theory derived for a monodisperse population of scatterers [18,19], the structure function is fit to $\Delta(q,\tau) = A(q)\{1 - \exp[-\tau/\tau_0(q)]\} + B(q)$, where $A(q)$ is a prefactor that depends on the generalized optical transfer function of the optical setup, $B(q)$ is the background, and $\tau_0(q)$ is the characteristic relaxation time of the scatterers at a wave vector q. Here we modified the standard DDM fitting function to model a polydisperse population of scatterers and fitted $\Delta(q,\tau)$ of the protein cluster solutions at each q using a modified cumulant fit [42]

$$\Delta(q,\tau) = A(q)\left[1 - \exp\left(-\frac{\tau}{\tau_c(q)}\right)\left(1 + \frac{\mu\tau^2}{2}\right)\right] + B(q), \tag{1}$$

where $\tau_c(q)$ is the wave-vector-dependent cluster relaxation time and $\mu\tau_c^2$ is a measure of the relative polydispersity of the cluster population. The use of the polydisperse cumulant function allowed us to describe curvature in $\Delta(q,\tau)$ at the shortest time scales that could not be well fit using a single-exponential model (Fig. 8 in Appendix A). We found that $\tau_c^{-1} \propto q^2$ and thus the diffusion coefficient D_c was evaluated as the slope of the straight line τ_c^{-1} versus q^2 (i.e., $\tau_c^{-1} = D_c q^2$).

The range of wave vectors was determined by the optical properties of the experimental setup. The minimal accessible wave vector was $q_{\min} = 2\pi/l$, where l was the largest dimension of the original images that were captured by the camera; using the typical $l = 140$ μm, $q_{\min} = 0.045$ μm^{-1}. The maximum accessible wave vector was $q_{\max} = 2\pi/\Delta l$, where Δl was the pixel dimension in the space of the image; using the typical $\Delta l = 0.21$ μm, $q_{\max} = 28.7$ μm^{-1}. In practice, $q_{\max}$ was limited by the smallest resolvable distance that a cluster could travel between two frames; we found that $q_{\max} = \min\{q',q''\}$, where $q' = \sqrt{\mathcal{F}/D}$ and $q'' = 2\pi n \sin(\theta_{\max})/\lambda$, where $n = 1.331$ is the refractive index of water.

C. Dynamic light scattering

Light scattering data were collected with an ALV goniometer equipped with a He-Ne laser (632.8 nm) and an ALV-5000/EPP Multiple tau Digital Correlator (ALV-GmbH, Langen, Germany). For light scattering experiments samples were placed in cylindrical cuvettes of diameter 10 mm; to minimize contamination, all cuvettes were washed with soap and rinsed with copious amounts of DI water prior to loading into the DLS instrument. Thirty intensity correlation functions were acquired at 90° for 60 s each to obtain an average intensity-intensity correlation function $g_2(\tau)$ at lag times τ ranging from 0.1 μs to 10 s. Light is scattered by the fluctuations of concentration and the correlation function characterizes the rate of diffusion of scatterers during decay of fluctuations [43]. Protein solutions typically contain two scatterers with distinct diffusion times, protein monomers, and protein-rich clusters [31,33,34,44,45]. We therefore determined the characteristic diffusion times τ_m and τ_c of the monomers and clusters, respectively, by fitting the normalized correlation function with a square sum of two terms, a single-exponential function corresponding to the monomer population and a modified cumulant function [42,46] to model the polydisperse cluster population

$$g_2(\tau) - 1 = \left[A_m \exp\left(-\frac{\tau}{\tau_m}\right) + A_c \exp\left(-\frac{\tau}{\tau_c}\right)\left(1 + \frac{\mu\tau^2}{2}\right)\right]^2 + \epsilon(\Delta t), \tag{2}$$

where A_m and A_c are related to the concentration of monomers and clusters, $\mu\tau_c^2$ characterizes the relative polydispersity of the clusters, and $\epsilon(\tau)$ accounts for inevitable noise [45]. We used τ_c to determine the cluster diffusivity D_c from $\tau_c^{-1} = D_c q^2$, where $q = (4\pi n/\lambda)\sin(\theta/2)$ is the scattering wave vector at 90°C, $\lambda = 632.8$ nm is the wavelength of the incident red laser, and $n = 1.331$ is the refractive index of DI water.

D. Calculation of the characteristic cluster size

We determined the average cluster radius R_c from D_c (measured using DDM or DLS) using the Stokes-Einstein equation

$$R_c = \frac{k_B T}{6\pi\eta D_c}, \tag{3}$$

where k_B is the Boltzmann constant, T is the temperature, and η is the viscosity of the protein and cluster solution. Determinations of the viscosity are made on solutions containing proteins and clusters; the volume fraction of clusters is less than 10^{-5} and hence the clusters negligibly affect the background viscosity. In lysozyme solutions (103 mg ml^{-1}) this viscosity is determined from the dynamics of Optilink carboxylated polystyrene spheres with diameter $2R = 0.424$ μm, characterized by DLS, and Eq. (3) [31]. For hemoglobin A (50 mg ml^{-1}), the solution viscosity was calculated using the relation [47]

$$\eta = \eta_0 \exp\left(\frac{[\eta]C}{1 - (k/\nu)[\eta]C}\right), \tag{4}$$

where $\eta_0 = 0.937$ mPa s is the viscosity of the phosphate buffer at 25°C, $[\eta] = 0.036$ dl g^{-1} is the viscosity increment, C is the HbA concentration in g dl^{-1}, k is a crowding factor, and ν is a shape factor coefficient for nonspherical particles so that $k/\nu = 0.42$ [47]. For hemoglobin at $C = 50$ mg ml^{-1}, $\eta = 1.14$ mPa s; for lysozyme at $C = 103$ mg mg^{-1}, $\eta = 1.42$ mPa s.

III. RESULTS AND DISCUSSION

A. Characterization of protein-rich clusters with BDDM

We acquire optical microscopy movies of protein-rich liquid clusters, reported in a variety of protein solutions [30–38,48], diffusing in solution for two proteins in chambers of thickness 160 μm. Optical bright-field micrographs of a hemoglobin A solution at a concentration of 50 mg ml^{-1} show that the clusters are too small to be directly resolved [Fig. 1(a)]; the large black spots correspond to dust and dirt in the microscope optical train. Subtracting two micrographs that are separated by a fixed lag time τ generates an image with a diffuse speckle pattern, as shown in Figs. 1(b)–1(d). These image differences usually have limited dynamic range, with typical intensities in an 8-bit image ranging in absolute value from 1 to 20 (Fig. 9 in Appendix A). The fluctuations increase as the lag time separating the micrographs is increased, indicating that the cluster positions become increasingly decorrelated over time.

To characterize the dynamics of these clusters, we apply BDDM and investigate the behavior of the azimuthally averaged structure function $\Delta(q,\tau)$. At a constant lag time τ, $\Delta(q,\tau)$ exhibits a pronounced maximum at a particular wave vector q, as shown in Fig. 2 for a solution containing hemoglobin A clusters. The existence of the maximum is related to the optical transfer function and is characteristic of BDDM measurements [24]. Increasing the lag time shifts this maximum to lower q and its height increases, as also seen in other BDDM measurements [19].

At a constant scattering wave vector q, $\Delta(q,\tau)$ first increases monotonically at short lag times and reaches a plateau at long lag times, as shown for solutions containing hemoglobin A and lysozyme clusters in Figs. 3(a) and 3(b), respectively. For a fixed q, the structure function Δ can be fitted to a cumulant model (1), from which we extract the q-dependent characteristic relaxation time $\tau_c(q)$, signal coefficient $A(q)$, background term $B(q)$, and polydispersity $\mu\tau_c^2$. The background term $B(q)$ is nearly constant at all wave vectors and does not differ significantly between the two proteins (Fig. 10 in Appendix A), consistent with the suggestion that $B(q)$ depends on the electronic noise of the sensor and the power spectrum of the optical train of the microscope [19]. Hemoglobin A generates a measurable DDM signal for $q = 0.5$–$6.5\ \mu$m^{-1}; by contrast, lysozyme generates a measurable signal for a smaller range of wave vectors $q = 1$–3.7μm^{-1}. Here a measurable signal is one for which the quotient $A(q)/B(q)$, one metric of the signal-to-noise ratio [21], is greater than or equal to 0.055 (Fig. 11 in Appendix A). In the polydispersity term, μ is the second cumulant of the intensity-weighted diffusion time distribution and larger values of $\mu\tau_c^2$ (which is approximately independent

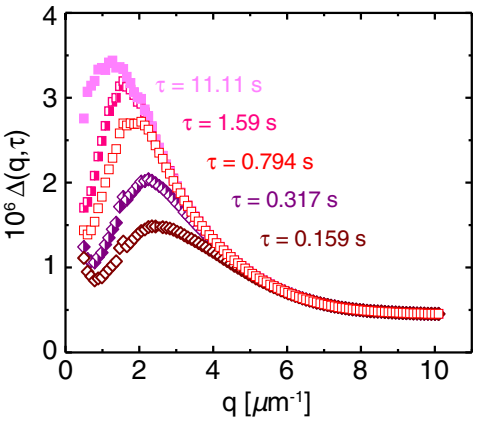

FIG. 2. (Color online) Structure function Δ as a function of wave vector q at lag times τ specified in the plot, obtained with bright-field differential dynamic microscopy for a hemoglobin A solution with a concentration of 50 mg ml^{-1}.

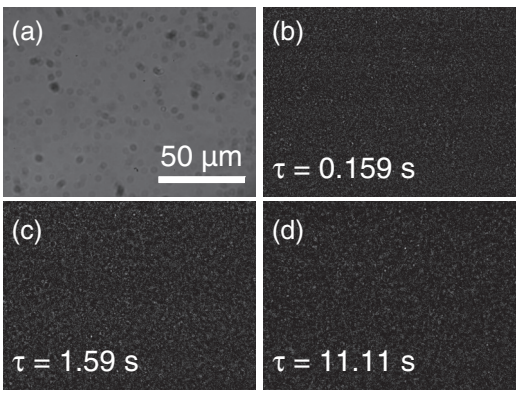

FIG. 1. (a) Representative bright-field micrograph of a hemoglobin A solution with a concentration of 50 mg ml^{-1}. (b)–(d) Representative subtractions of two images at lag times τ, as indicated in the panels. The scale bar for all images is shown in (a).

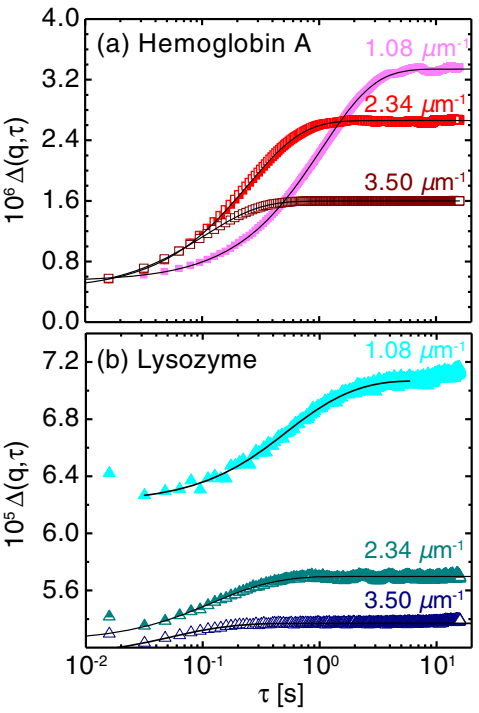

FIG. 3. (Color online) Structure function Δ as a function of lag time τ at three wave vectors q, indicated in the plots, for solutions of (a) hemoglobin A at a concentration of 50 mg ml^{-1} and (b) lysozyme at a concentration of 103 mg ml^{-1}. Lines are best fits to Eq. (1).

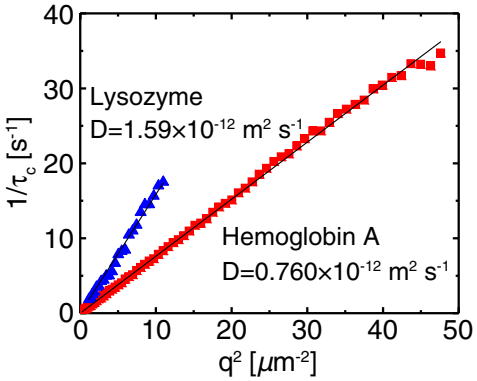

FIG. 4. (Color online) Reciprocal relaxation time $1/\tau_c$ as a function of the wave vector q for a hemoglobin A solution with a concentration of 50 mg ml^{-1} (squares) and lysozyme solution with a concentration of 103 mg ml^{-1} (triangles). Here τ_c scales as q^{-2} and the intercept is insignificant (linear fits pass through the origin), as expected for freely diffusing clusters.

of the scattering vector for $q > 1$, as shown in Fig. 12 in Appendix A) correspond to a more polydisperse cluster population. Here the lysozyme solutions are more polydisperse ($\mu\tau_c^2 \approx 0.16$) than the hemoglobin A solutions ($\mu\tau_c^2 \approx 0.075$). For both proteins, the reciprocal relaxation time $1/\tau_c(q)$ scales linearly with q^2 (Fig. 4) and a linear fit goes through the origin. These features indicate that the dynamics of the clusters is purely diffusive. We calculate the average diffusion coefficient for each cluster from the slope of the fit line and obtain $D_c = 0.760 \times 10^{-12}$ and 1.59×10^{-12} m^2 s^{-1} for hemoglobin A and lysozyme clusters, respectively. From the Stokes-Einstein equation (3) where η is the viscosity of the protein solution, the characteristic radii of hemoglobin A and lysozyme clusters are 232 and 95 nm, respectively. The hemoglobin A clusters are larger and thus scatter more light, leading to a greater DDM signal-to-noise ratio as compared to that of lysozyme clusters, consistent with the structure functions shown in Fig. 3.

B. Do thicker chambers yield a stronger DDM signal?

The DDM measurements reported in Figs. 2 and 3 are performed in thin chambers of thickness ~160 μm. Many biological samples are difficult to purify or obtain in large volumes and so the use of thinner chambers and hence smaller sample volumes is desirable. The bright-field DDM method generates signal from a thickness that is greater than the focal volume of the optical train but can be limited by the sample thickness. The minimum sample thickness required to neglect finite-size effects in the DDM signal is $L_{\min} > 1/\Delta q$, where Δq is the uncertainty in the scattering wave vector due to the finite numerical aperture of the condenser and the polychromaticity of the illumination source [19]. We calculate $(\Delta q/q)^2 \approx 0.0307$ using the expression from Ref. [19] and obtain $L_{\min} = 11$ μm and 0.83 μm at the minimum and maximum q of 0.5 and 6.5 μm^{-1}, respectively, accessible with hemoglobin A solutions. We can therefore neglect finite-size effects for chambers whose thickness exceeds 11 μm.

To determine the chamber thickness required to generate signal in DDM for weakly scattering protein clusters, we

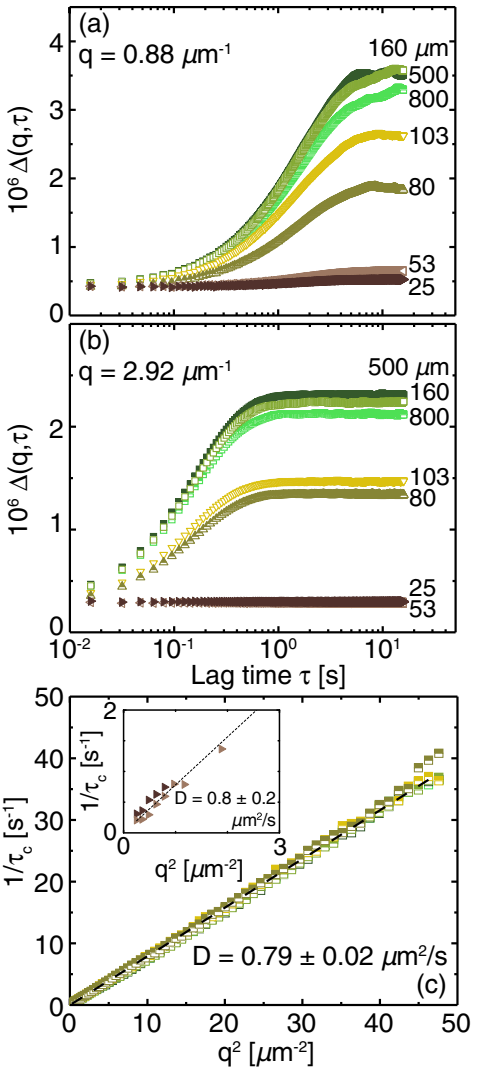

FIG. 5. (Color online) Structure function $\Delta(q,\tau)$ as a function of lag time τ for a hemoglobin A solution at a concentration of 50 mg ml^{-1}, measured in chambers of indicated thicknesses, at wave vector (a) $q = 0.88\mu$m^{-1} and (b) $q = 2.92\,\mu$m^{-1}. (c) Reciprocal relaxation time $1/\tau_c$, obtained from the fit of $\Delta(q,\tau)$ to Eq. (1), as a function of the wave vector q for a hemoglobin A solution with a concentration of 50 mg ml^{-1} measured in chambers of varying thickness; symbols and colors correspond to those used in (a) and (b). The inset shows the same dependence for the two thinnest chambers (of thicknesses 25 and 53 μm), showing that the noisy and weak BDDM signal can be measured only for a limited range of q.

measure the intensity differences (Fig. 13 in Appendix A) and the image structure function $\Delta(q,\tau)$ for hemoglobin clusters in chambers of thickness ranging from 25 to 800 μm, for which we expect finite-size effects to be negligible. The dependence on chamber thickness arises from the fact that planes farther from the object plane contribute progressively less to the DDM signal [19]. At a low wave vector ($q = 0.88\,\mu$m^{-1}) the signal above the noise [i.e., $A(q)/B(q)$] is sufficiently large, allowing each $\Delta(q,\tau)$ to be fit to Eq. (1) and the relaxation time scale $\tau_c(q)$ to be extracted [Fig. 5(a)] [21]. At higher wave vectors, however, $A(q)/B(q) < 0.055$ for the thinnest sample chambers and these $\Delta(q,\tau)$ cannot be fit to

Eq. (1) [Fig. 5(b)]. Reducing the chamber thickness below $\sim$160 μm restricts the range of wave vectors from which $\tau_c(q)$ can be extracted, in accord with the theoretical prediction from Ref. [19]. Nonetheless, over the accessible range of wave vectors for each thickness the inverse relaxation time $1/\tau_c(q)$ scales with q^2; moreover, all points lie on a single line, confirming that the diffusion coefficient of the clusters remains constant across chambers of different thickness. This result suggests that there exists an optimal chamber thickness for biological samples (here $\sim$160 μm for hemoglobin A solutions), which minimizes the total sample volume while still allowing the maximum range of wave vectors to be accessed. This optimal thickness, which must depend on the properties of the sample and of the optical setup, can be determined from the ratio of the signal to noise $A(q)/B(q)$ (shown in Fig. 14 in Appendix A). We found that the signal-to-noise criterion $A(q)/B(q) \geqslant 0.055$ established for bulk solutions also applies to the thickness measurements; only those thicknesses and wave vectors satisfying this criterion yield relaxation times that scale diffusively with the cluster size.

C. Comparison with DLS

To verify the diffusion coefficients and cluster sizes obtained using BDDM, we measure the characteristic relaxation time scale using DLS at a single scattering angle of 90° in a cuvette of internal diameter of 8 mm. The dynamic correlation functions $(g_2 - 1)^{1/2}$ of hemoglobin A [Fig. 6(a)] and of lysozyme [Fig. 6(b)] solutions exhibit two distinct relaxations, indicating the presence of objects of two different characteristic sizes. From fitting each dynamic correlation function using the method of cumulants (2) we obtain the characteristic relaxation time of the (polydisperse) clusters [45] τ_c. Using the Stokes-Einstein equation (3), we calculate an average radius of 144 and 72 nm, respectively, for hemoglobin A and lysozyme clusters; these values are in agreement with previous determinations for both proteins [31,33]. Notably, the characteristic sizes for hemoglobin A (232 nm) and lysozyme (95 nm) determined using DDM are greater than those determined using DLS.

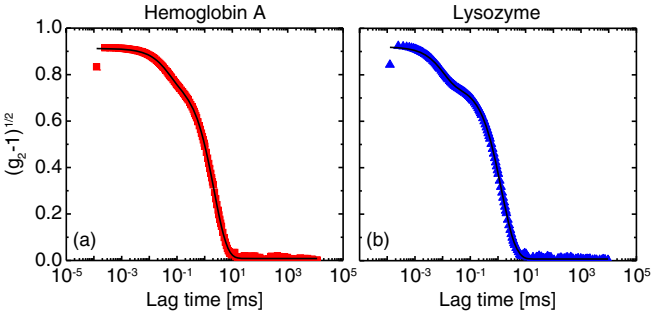

FIG. 6. (Color online) Autocorrelation function $(g_2 - 1)^{1/2}$ of scattered light as a function of lag time τ for (a) a hemoglobin A solution with a concentration of 50 mg ml^{-1} and (b) a lysozyme solution with a concentration of 103 mg ml^{-1}. All dynamic light scattering measurements were performed at a detector angle of 90°, corresponding to a scattering vector $q = 18.7$ μm^{-1}.

We consider several potential origins for the discrepancy between the sizes measured by DDM and by DLS. First, in earlier experiments [21] we showed that DLS and DDM experiments on monodisperse polymer particles of radii 50–200 nm yield identical particle sizes; this finding suggests that collective motion within the sample chambers does not lead to the observed discrepancy. Second, the relative polydispersities at higher q are equal within errors of each measurement (Fig. 12 in Appendix A), suggesting that the discrepancy does not arise from differences in the sensitivities of the camera used in the DDM experiment and of the correlator used in the DLS experiment. Finally, the decorrelation times measured in DDM (Figs. 4 and 5) and in DLS [38] both scale diffusively with the wave vector, i.e., $1/\tau \propto q^2$, as expected for a dilute suspension of spherical scatterers; this result suggests that any asphericity of the clusters does not give rise to the discrepancy.

D. Effect of polydispersity on apparent cluster sizes

Instead, we apply Mie theory to understand the origin of the discrepancy between the sizes from DDM and DLS. First, we show that the Mie scattering limit is applicable to these systems. For a particle of diameter $2R$ interacting with light of wavelength λ in a medium of refractive index n, the size parameter $x = 2\pi Rn/\lambda$ determines the relevant scattering limit: Mie scattering applies for $x > 0.4$. The illumination source used in the microscopy experiments has a broad distribution of wavelengths; using an average wavelength of $\lambda_0 = 550$ nm for the incident white light, $x = 2.18$ and 1.09 for hemoglobin A and lysozyme clusters, respectively. The size of the particles is comparable to the wavelength of incident light and so we consider the Mie solution to Maxwell's equations, which describes the scattering of an incident plane wave from a collection of spheres. The Mie solution is written as a series expansion in terms of spherical harmonic functions [49], which in turn are typically expressed in terms of the associated Legendre polynomials $P_l^m(\cos\theta) = \frac{(1-\cos^2\theta)^{m/2}}{2^l l!}\frac{d^{l+m}(\cos^2\theta-1)^l}{d(\cos\theta)^{l+m}}$. The angular dependence of the Mie angular functions $\pi_n(\cos\theta) = (1/\sin\theta)P_l^m(\cos\theta)$ and $\tau_n(\cos\theta) = dP_l^m(\cos\theta)/d\theta$ thus determines the intensity of scattered light as a function of the scattering angle [50]. The function π_n exhibits fore-aft symmetry for even n, with lobes directed forward (i.e., 0°) and backward (i.e., 180°); for odd n, however, the backward lobe vanishes. Similarly, τ_n exhibits fore-aft symmetry for odd n, but the backward lobe vanishes for even n. This angular dependence leads to a forward-directed bias in the scattering intensity that becomes more pronounced as the index l is increased. Furthermore, as the size of the scattering objects is increased, more terms in the series expansion are incorporated in the scattering diagram [51]. Larger scatterers, which scatter more strongly overall, also preferentially scatter more in the forward direction compared to smaller scatterers.

We employ a Mie scattering model [52] to estimate the difference in magnitude of the intensity of forward-scattered and laterally scattered light for hemoglobin A clusters. (Additional details on the Mie scattering model calculations are given in Appendix B.) Our DLS experiments use homodyne detection, in which only the scattered light is captured by the photodetector. By contrast, DDM is a heterodyne near-field scattering

method: the light scattered from the clusters interferes with the transmitted light. Hence in DDM the intensity of scattered light is proportional to the scattered electrical field [53]. To confirm that the heterodyne condition was satisfied for our experiments, we calculated the distributions of the intensity difference. The distributions of the intensity difference were Gaussian at all τ, confirming that the heterodyne condition was satisfied (Fig. 9 in Appendix A).

Still, the DDM structure function is derived from fluctuations in intensity. Under the Gaussian approximation, valid for these experiments, the DDM structure function is proportional to the square of the scattered electrical field, as in homodyne DLS, and hence proportional to the scattered intensity. (A short derivation applicable to our experiment is given in Appendix C.) Indeed, Giavazzi *et al.* pointed out that $\Delta(\mathbf{q},\tau)$ is the two-dimensional generalization of the photon structure function measured in DLS experiments [19]. In our experiments, the homodyne and heterodyne detection schemes contain the same information and we therefore use the Mie model for both the DDM and DLS signals.

For calculations of the DLS scattering intensity, we use the excitation wavelength of $\lambda = 633$ nm in our experimental DLS setup and a scattering angle of 90°. For calculations of the DDM scattering intensity, following Ref. [19] we assume that the distribution of wavelengths in the illumination source can be described by a Gaussian function centered at a wavelength $\lambda_0 = 550$ nm. At a scattering angle of 90°, the intensity of scattered light exhibits a local maximum at a particular radius [Fig. 7(a)], arising from morphological resonances due to constructive interference [51]. At a scattering angle of 0° the intensity monotonically increases with radius [Fig. 7(b)]. For a given particle radius, the scattered intensity is greater at 0° than at 90°, as expected in the Mie scattering regime. The DDM experiments for hemoglobin A access scattering angles ranging from approximately 1.8 to 24.5 degrees, as calculated from the minimum and maximum scattering vectors $q = 0.5$ and 6.5 μm^{-1} via $q = (4\pi n/\lambda_0)\sin(\theta/2)$. We therefore also report the Mie scattering intensity at an angle of 24° [Fig. 7(c)].

The protein-rich liquid clusters are not monodisperse but instead exhibit a distribution of sizes. To assess the effect of cluster size polydispersity on the DDM signal intensity, we assume that the cluster size distribution can be described by a Gaussian function of characteristic width σ that is centered near the average radius of hemoglobin A clusters measured using DLS, $R_c = 140$ nm. We sum the Mie scattering intensities for hemoglobin A clusters of each radius, weighted by the Gaussian function, and thereby obtain the scattered intensity for a polydisperse distribution of cluster sizes. When the characteristic width σ is small ($\sigma/R_c \approx 0.016$), the distributions of scattered intensity at 0°, at 24°, and at 90° strongly overlap with the distribution of cluster radii [Fig. 7(d)], indicating that the characteristic radius measured at each angle is nearly identical. By contrast, when the cluster radii are more broadly distributed ($\sigma/R_c \approx 0.28$) the position of the maximum in scattering intensity is shifted to larger radius compared to that of the Gaussian radius distribution N, as shown in Fig. 7(e). Moreover, this shift is more pronounced at scattering angles of 0° and 24°, corresponding to the angular range accessed in the DDM experiments, than at 90°, corresponding to the angle in the DLS experiments. This result indicates

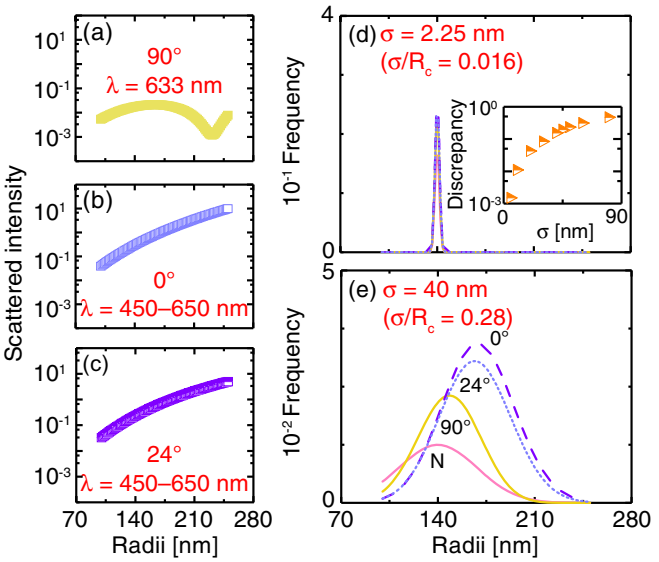

FIG. 7. (Color online) (a)–(c) Scattered intensity of hemoglobin A clusters as a function of cluster radius predicted using Mie scattering theory for (a) dynamic light scattering, using a wavelength $\lambda = 633$ nm and a scattering angle of $\theta = 90°$; (b) BDDM, using a wavelength range $\lambda = 450$–650 nm and a scattering angle of $\theta = 0°$; and (c) BDDM, using a wavelength range $\lambda = 450$–650 nm and a scattering angle of $\theta = 24°$. (d) and (e) Calculated scattered intensity distributions containing clusters with a Gaussian size distribution N centered at 140 nm and of width (d) $\sigma = 2.25$ nm ($\sigma/R_c = 0.016$) and (e) $\sigma = 40$ nm ($\sigma/R_c = 0.28$). The inset in (d) shows the discrepancy between the peak positions predicted for DLS and DDM as a function of size distribution width σ.

that polydispersity can generate the discrepancy between the DDM and DLS characteristic sizes. We quantify the predicted discrepancy between the characteristic sizes measured using BDDM and DLS as $(R_{c,\text{DDM}} - R_{c,\text{DLS}})/R_{c,\text{DLS}}$ for the 0° scattering intensity and the 90° scattering intensity and find that this discrepancy increases monotonically with σ [inset in Fig. 7(d)]. As the cluster size distribution broadens, the characteristic size measured by DDM becomes progressively larger compared to that measured by DLS.

IV. CONCLUSION

We showed that DDM can be used to monitor the dynamics of weakly scattering and polydisperse biological nanoscale objects, protein-rich liquid clusters, and to characterize the sizes of the clusters. Increasing the thickness of the sample chamber enhances the signal from weakly scattering objects and hence increases the range of wave vectors accessible with DDM; increasing above a certain thickness, here approximately 160 μm for hemoglobin A, produces no further increase in the DDM signal. We noted that the optimal thickness must depend on the concentration, size, and refractive index mismatch of the scatterers and on the bit depth of the camera. The characteristic size measured by DDM was consistently larger than that measured by DLS at a scattering angle of 90°. Using the Mie scattering solution, we showed that larger clusters preferentially contribute to the low-angle DDM signal, leading to a bias towards longer relaxation times and hence

larger average sizes. This bias increases with the width of the cluster size distribution. This result neglects absorption from the clusters or scattering medium, which does not significantly affect the accuracy of data collected using scattering methods; for example, the slight absorption of hemoglobin A does not affect cluster sizes measured using DLS [54] and we expect that it also does not significantly alter the shift in characteristic size using DDM.

Although here we focused on the dynamics of a well-characterized model system, our results are broadly applicable for polydisperse nanoparticles that weakly scatter light. Weakly polydisperse protein clusters exhibit near-exponential decays in DDM. This result is in contrast to the stretched exponential dynamics of nanoparticles in homogeneous porous media measured using DDM [28], which may reflect local environmental heterogeneity [55]. This comparison suggests that DDM could be used to identify the physical origins of dynamical processes. When combined with optical methods used for concentrated suspensions [20] or extended analyses used for nonspherical objects [24,27], we therefore expect that DDM will provide a simple, inexpensive, and rapid method to characterize the diffusive dynamics of a broad range of polydisperse nanoparticles in complex biological environments.

ACKNOWLEDGMENTS

We thank Anupam Aich for help with hemoglobin purification and solution preparation, Rahul Pandey for introduction to DDM, and Kai He and Jack Jacob for assistance with image and data processing. We additionally thank two anonymous referees for insightful suggestions. This work was supported by NASA (Grant No. NNX14AD68G to P.G.V. and J.C.C.) and NSF (Grants No. MCB-1244568 to P.G.V. and No. DMR-1151133 to J.C.C.).

APPENDIX A: SUPPLEMENTAL FIGURES

In this Appendix we provide additional figures (Figs. 8–14) to justify statements made in the main text. In Fig. 8 we show that the DDM data cannot be adequately fit with a single-exponential fitting model. In Fig. 9 we show that the histograms of intensity difference values (which have limited dynamic range) can be fitted by a Gaussian distribution, satisfying the heterodyne condition. In Fig. 10 we show that the background term $B(q)$ is nearly constant at all wave vectors and does not differ significantly between the two proteins. In Fig. 11 we show that the criterion for a measurable signal in our DDM setup is $A(q)/B(q) \geqslant 0.055$. In Fig. 12 we show that the relative polydispersity is approximately independent of the scattering wave vector for $q > 1\ \mu\mathrm{m}^{-1}$. In Fig. 13 we show the histograms of absolute intensity difference measured for a solution of hemoglobin A in chambers of thickness ranging from 25 to 800 μm. Finally, in Fig. 14 we show that the criterion for a measurable signal established in Fig. 11, $A(q)/B(q) \geqslant 0.055$, is also valid for chambers of varying thickness.

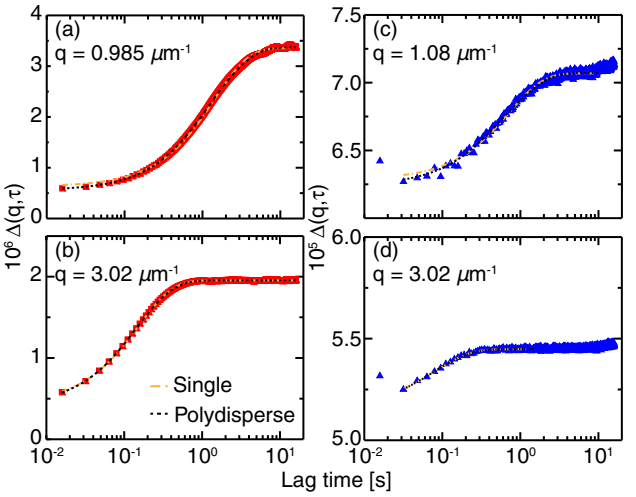

FIG. 8. (Color online) Structure function Δ as a function of lag time τ at wave vectors q, indicated in the plots, for (a) and (b) a hemoglobin A solution with a concentration of 50 mg ml^{-1} and (c) and (d) a lysozyme solution with a concentration of 103 mg ml^{-1}. Orange dash-dotted lines indicate fits to a single exponential fitting function and black dotted lines indicate fits to a polydisperse cumulant fitting model. At low q the single-exponential model systematically overestimates the short-time plateau and a polydisperse exponential model (1) gives a better fit.

APPENDIX B: MIE SCATTERING CALCULATIONS

The Mie scattering solution of Maxwell's equations, first developed by Lorenz [56] and independently by Mie [49], describes the relation between transverse components of electric and magnetic fields of scattered electromagnetic wave from a dielectric (potentially absorbing) spherical particle of radius R with respect to incident fields of electromagnetic wave. The Mie solution assumes that the tangential components of the electric and magnetic fields are continuous across the surface of the spherical particle. The resulting components of the

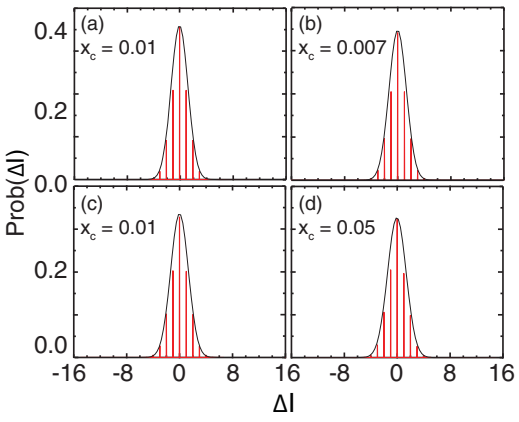

FIG. 9. (Color online) Histogram of intensity difference values measured at lag times of (a) 0.015 87 s, (b) 0.1587 s, (c) 1.587 s, and (d) 15.87 s for a hemoglobin A solution with a concentration of 50 mg ml^{-1}. Black lines indicate Gaussian fits to each distribution, with the centroid of the Gaussian indicated in each panel, confirming that the heterodyne condition is satisfied for these data sets.

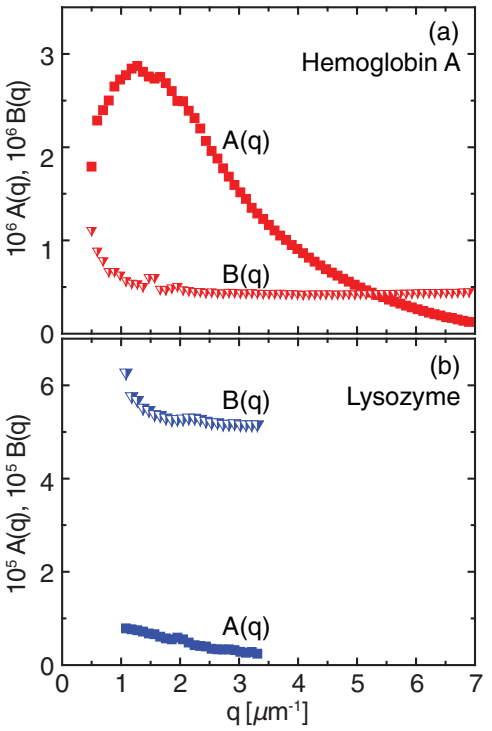

FIG. 10. (Color online) Parameters $A(q)$ and $B(q)$ determined from fits of experimental data to Eq. (1), as a function of scattering wave vector q for (a) hemoglobin A with a concentration of 50 mg ml^{-1} and (b) lysozyme with a concentration of 103 mg ml^{-1}.

scattered electric and magnetic fields are described in terms of an infinite series expansion of vector spherical harmonics. For a detailed derivation of the Mie solution, see Ref. [50]; here, we give only the formulas needed for a computational Mie approach.

For an incident plane wave, the scattering amplitudes in the Mie solution $S_1(\theta)$ and $S_2(\theta)$ are given by

$$S_1(\theta) = \sum_{n=1}^{\infty} \frac{2n+1}{n(n+1)} [a_n \pi_n(\cos\theta) + b_n \tau_n(\cos\theta)] \qquad \text{(B1)}$$

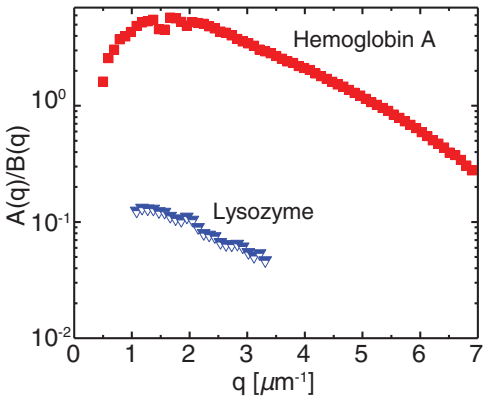

FIG. 11. (Color online) Ratio of the fit parameters $A(q)/B(q)$, a measure of the signal-to-noise ratio, as a function of scattering wave vector q for a hemoglobin A solution with a concentration of 50 mg ml^{-1} and a lysozyme solution with a concentration of 103 mg ml^{-1}.

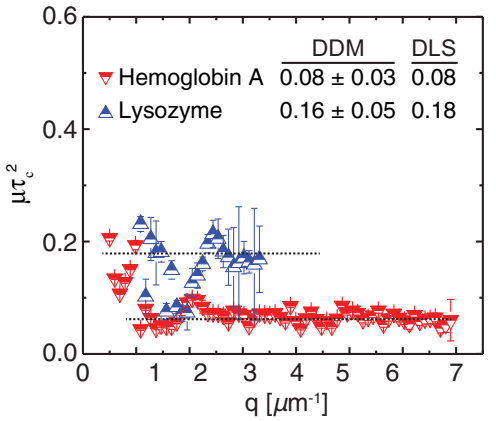

FIG. 12. (Color online) Relative polydispersity $\mu\tau_c^2$ as a function of the scattering wave vector q for a hemoglobin A solution with a concentration of 50 mg ml^{-1} and a lysozyme solution with a concentration of 103 mg ml^{-1} measured using DDM. Dashed lines indicate the average polydispersity. The inset shows a comparison of average relative polydispersity from the DDM and DLS measurements; the errors given for the DDM measurements indicate the standard deviation of the values obtained at different q. Within the reported error, the polydispersities measured in DLS and DDM are identical.

and

$$S_2(\theta) = \sum_{n=1}^{\infty} \frac{2n+1}{n(n+1)} [a_n \tau_n(\cos\theta) + b_n \pi_n(\cos\theta)]. \qquad \text{(B2)}$$

The Mie angular functions $\pi_n(\cos\theta)$ and $\tau_n(\cos\theta)$ describe the angular dependence of the scattering radiation and are given in terms of the associated Legendre polynomials P_n^1 as

$$\pi_n(\cos\theta) = \frac{1}{\sin\theta} P_n^1(\cos\theta) \qquad \text{(B3)}$$

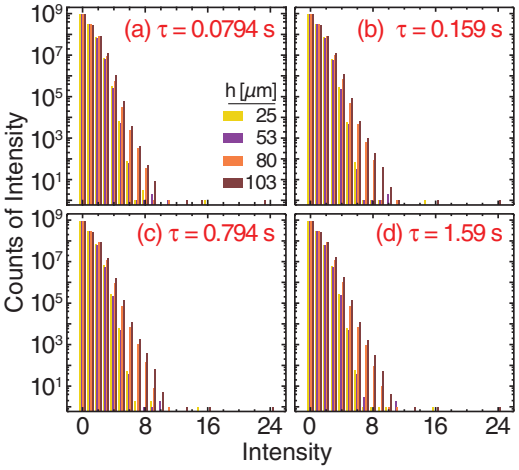

FIG. 13. (Color online) Histogram of absolute intensity difference values measured for a hemoglobin A solution with a concentration of 50 mg ml^{-1} in chambers of different thickness at the lag times indicated in the plots.

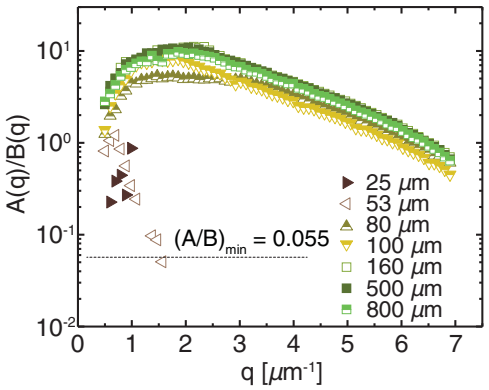

FIG. 14. (Color online) Ratio of the fit parameters $A(q)/B(q)$, a measure of the signal-to-noise ratio, as a function of scattering wave vector q for a hemoglobin A solution with a concentration of 50 mg ml^{-1} in chambers of varying thickness. The signal-to-noise criterion identified for bulk signals $A/B = 0.055$ is indicated as a dashed line in the figure.

and

$$\tau_n(\cos\theta) = \frac{d}{d\theta} P_n^1(\cos\theta). \tag{B4}$$

The scattering coefficients a_n and b_n are obtained by matching the tangential electric and magnetic fields at the surface of the dielectric sphere (at $r = R$). These coefficients are typically given in terms of the Ricatti-Bessel functions ψ_n and ξ_n [50] as

$$a_n = \frac{m\psi_n(mx)\psi_n'(x) - \psi_n(x)\psi_n'(mx)}{m\psi_n(mx)\xi_n'(x) - \xi_n(x)\psi_n'(mx)} \tag{B5}$$

and

$$b_n = \frac{\psi_n(mx)\psi_n'(x) - m\psi_n(x)\psi_n'(mx)}{\psi_n(mx)\xi_n'(x) - m\xi_n(x)\psi_n'(mx)}, \tag{B6}$$

where $m = n - i\kappa$ is the complex index of refraction and $x = 2\pi Rn/\lambda$ is the Mie size parameter for a particle of radius R scattering light of wavelength λ in a medium of refractive index n. The Ricatti-Bessel functions are defined as

$$\psi_n(z) = \left(\frac{\pi z}{2}\right)^{1/2} J_{n+1/2}(z) \tag{B7}$$

and

$$\xi_n(z) = \left(\frac{\pi z}{2}\right)^{1/2} H_{n+1/2}(z). \tag{B8}$$

In Eqs. (B7) and (B8), $J_{n+1/2}(z)$ is the half-integer-order Bessel function of the first kind and $H_{n+1/2}(z)$ is the half-integer-order Hankel function of the second kind.

In the far field, the transverse components of the scattered electric field are given by [50]

$$E_{s\theta} \sim E_0 \frac{e^{ikr}}{-ikr} \cos\phi S_2(\cos\theta) \tag{B9}$$

and

$$E_{s\phi} \sim E_0 \frac{e^{ikr}}{-ikr} \sin\phi S_1(\cos\theta), \tag{B10}$$

where $e^{ikr}/(-ikr)$ represents the outgoing spherical wave. Finally, the scattered intensity parallel to the scattering plane is $I_1 = I_\parallel = |S_2|^2$ and that perpendicular to the scattering plane is $I_2 = I_\perp = |S_1|^2$, with the total scattering intensity thus given by $I = I_1 + I_2$. This calculation is true not only for our (homodyne) DLS setup, but also for our (double-frame heterodyne) DDM setup, as we have shown that the DDM structure function is also proportional to the scattering intensity (C10).

In a typical Mie scattering algorithm, the coefficients a_n and b_n are first calculated for values of $n = 1, \ldots, N$, where $N \approx x + 4x^{1/3} + 2$ [50]. Next, the functions $\pi_n(\cos\theta)$ and $\tau_n(\cos\theta)$ are calculated using the recursion relations for the associated Legendre polynomials. Finally, the scattering amplitudes $S_1(\theta)$ and $S_2(\theta)$ are calculated as a function of the scattering angle θ. In our calculations we use the MATLAB functions for Mie scattering and absorption by Mätlzer [52] and report the total scattering intensity I.

APPENDIX C: RELATIONSHIP OF THE DDM SIGNAL TO THE SCATTERING INTENSITY

Differential dynamic microscopy originated in the double-frame analysis in heterodyne near-field scattering (HNFS) [53]. Briefly, the DDM method is based on the Fourier analysis of the intensity image differences [19]. The key idea for DDM (as for all near-field scattering methods) is that the Fourier components of the intensity distribution in the image differences can be put in one-to-one correspondence with the Fourier components in terms of the sample refractive index [19].

Let $I(r,t_1)$ and $I(r,t_2)$ be the intensity of images at times t_1 and t_2 separated by a time difference $\tau = t_2 - t_1$. In the DDM analysis, the intensity difference between these two images is first calculated as

$$\delta I_t(r;\tau) = |I(r,t_2) - I(r,t_1)|. \tag{C1}$$

This process removes the potentially large and heterogeneous background signal. Next, the Fourier power spectrum of the intensity difference $\delta I_t(r;\tau)$, a robust statistical estimator of the energy content [57], is calculated as

$$|\delta\hat{I}_t(q;\tau)|^2 = \left|\int [\delta I_t(r;\tau)] e^{-qr} dr\right|^2. \tag{C2}$$

Finally, the expectation value of this spectrum is calculated by averaging over all starting times t_1 to generate the structure function

$$\Delta(q;\tau) = \langle|\delta\hat{I}_t(q,\tau)|^2\rangle. \tag{C3}$$

The DDM structure function $\Delta(q;\tau)$ is the two-dimensional generalization of the photon structure function in DLS [18,19]. Hence, for Brownian diffusion of a population of monodisperse scatterers, $\Delta(q;\tau)$ obtained from the DDM analysis can be fitted with a single-exponential function to extract the diffusion time of particles, just as the square root of the intensity-intensity correlation function can be fitted with a single-exponential function to extract the diffusion time of monodisperse particles in DLS. Below we show that $\Delta(q;\tau)$ is proportional to the intensity of the scattering field $I_s(r)$, which

is enhanced by a static prefactor equal to the intensity of the transmitted beam $I_0(r)$. The intensity of the scattered light is directly proportional to concentration fluctuations, which are caused by the Brownian motion of particles.

Next we show how to extract the DDM signal from a double-frame HNFS analysis. In HNFS [53], the static electric field $E_0(r)$ corresponding to the transmitted beam interferes with the time-dependent weak scattered field $E_s(r,t)$ to produce the transmitted field

$$E_t(r,t) = E_0(r) + E_s(r,t). \tag{C4}$$

The intensity of the transmitted beam $I_t = |E_t(r,t)|^2$ can be written as

$$I_t(r,t) = E_t(r,t)\overline{E_t}(r,t), \tag{C5}$$

where $\overline{E}$ is the complex conjugate of E. Substituting Eq. (C4) and neglecting the scattered intensity (which is small compared to the transmitted intensity), the intensity at a given time t is

$$I_t(r,t) = E_0(r)\overline{E_0}(r) + E_0(r)\overline{E_s}(r,t) + \overline{E_0}(r)E_s(r,t). \tag{C6}$$

The static transmitted intensity can be eliminated by calculating the intensity difference $\delta I_t(r,\tau) = I_t(r,t+\tau) - I_t(r,t)$. Thus $\delta I_t(r,\tau)$ can be written in terms of the scattered electric field $E_s(r,\tau) = E_s(r,t_2) - E_s(r,t_1)$ as

$$\delta I_t(r,\tau) = E_0(r)\overline{E_s}(r,\tau) + \overline{E_0}(r)E_s(r,\tau). \tag{C7}$$

Equation (C7) can be transformed to Fourier space. By applying properties of Fourier transforms, it can be shown that the Fourier transform of the intensity difference can be written as

$$\delta\hat{I}_t(q,\tau) = E_0(q) * [\overline{E_s}(-q,\tau) + E_s(q,\tau)]. \tag{C8}$$

Finally, the spectrum of the double-frame heterodyne signal $|\delta\hat{I}_t(q,\tau)|^2$ can be calculated from Eq. (C8), yielding

$$\begin{aligned}|\delta\hat{I}_t(q,\tau)|^2 = I_0(q)[&\overline{E_s}(-q,\tau) * E_s(-q,\tau)\\ &+ E_s(q,\tau) * \overline{E_s}(q,\tau) + \overline{E_s}(-q,\tau) * \overline{E_s}(q,\tau)\\ &+ E_s(q,\tau) * E_s(-q,\tau)],\end{aligned} \tag{C9}$$

where $*$ indicates a convolution operation. The first two terms contain the scattered intensity, whereas the last two are shadowgraph terms. The shadowgraph terms are eliminated after averaging over all initial times t [58,59], leading to

$$\langle|\delta\hat{I}_t(q,\tau)|^2\rangle = I_0(q)I_s(q,\tau). \tag{C10}$$

By comparing Eqs. (C3) and (C10), we conclude that the DDM signal is proportional to the scattered intensity. We note that this analysis holds for the case when number fluctuations can be neglected (and hence is not applicable, for example, to the case of dilute scatterers in convective flow).

[1] Y. Guo, S. Jangi, and M. A. Welte, Mol. Biol. Cell **16**, 1406 (2005).

[2] C. P. Brangwynne, G. H. Koenderink, F. C. Mackintosh, and D. A. Weitz, Trends Cell Biol. **19**, 423 (2009).

[3] K. Barlan, M. J. Rossow, and V. I. Gelfand, Curr. Opin. Cell Biol. **25**, 483 (2013).

[4] G. Li, L.-K. Tam, and J. X. Tang, Proc. Natl. Acad. Sci. USA **105**, 18355 (2008).

[5] J. N. Wilking, V. Zaburdaev, M. De Volder, R. Losick, M. P. Brenner, and D. A. Weitz, Proc. Natl. Acad. Sci. USA **110**, 848 (2013).

[6] B. R. Thomas, A. A. Chernov, P. G. Vekilov, and D. C. Carter, J. Cryst. Growth **211**, 149 (2000).

[7] P. G. Vekilov, Cryst. Growth Des. **7**, 2796 (2007).

[8] P. G. Vekilov, O. Galkin, B. M. Pettitt, N. Choudhury, and R. L. Nagel, J. Mol. Biol. **377**, 882 (2008).

[9] S. Barua and S. Mitragotri, ACS Nano **7**, 9558 (2013).

[10] Q. Xu, N. J. Boylan, J. S. Suk, Y.-Y. Wang, E. A. Nance, J.-C. Yang, P. J. McDonnell, R. A. Cone, E. J. Duh, and J. Hanes, J. Control. Release **167**, 76 (2013).

[11] W. G. Kreyling, S. Hirn, W. Möller, C. Schleh, A. Wenk, G. Celik, J. Lipka, M. Schäffler, N. Haberl, B. D. Johnston, R. Sperling, G. Schmid, U. Simon, W. J. Parak, and M. Semmler-Behnke, ACS Nano **8**, 222 (2014).

[12] A. Parodi, S. G. Haddix, N. Taghipour, S. Scaria, F. Taraballi, A. Cevenini, I. K. Yazdi, C. Corbo, R. Palomba, S. Z. Khaled, J. O. Martinez, B. S. Brown, L. Isenhart, and E. Tasciotti, ACS Nano **8**, 9874 (2014).

[13] B. J. Berne and R. Pecora, *Dynamic Light Scattering: With Applications to Chemistry, Biology, and Physics* (Dover, New York, 2000).

[14] J. C. Crocker and D. G. Grier, J. Colloid Interface Sci. **179**, 298 (1996).

[15] S. C. Weber, A. J. Spakowitz, and J. A. Theriot, Phys. Rev. Lett. **104**, 238102 (2010).

[16] B. Huang, Curr. Opin. Chem. Biol. **14**, 10 (2010).

[17] F. Giavazzi and R. Cerbino, J. Opt. **16**, 083001 (2014).

[18] R. Cerbino and V. Trappe, Phys. Rev. Lett. **100**, 188102 (2008).

[19] F. Giavazzi, D. Brogioli, V. Trappe, T. Bellini, and R. Cerbino, Phys. Rev. E **80**, 031403 (2009).

[20] P. J. Lu, F. Giavazzi, T. E. Angelini, E. Zaccarelli, F. Jargstorff, A. B. Schofield, J. N. Wilking, M. B. Romanowsky, D. A. Weitz, and R. Cerbino, Phys. Rev. Lett. **108**, 218103 (2012).

[21] K. He, M. Spannuth, J. C. Conrad, and R. Krishnamoorti, Soft Matter **8**, 11933 (2012).

[22] F. Ferri, A. D'Angelo, M. Lee, A. Lotti, M. C. Pigazzini, K. Singh, and R. Cerbino, Eur. Phys. J. Spec. Top. **199**, 139 (2011).

[23] M. Reufer, V. A. Martinez, P. Schurtenberger, and W. C. K. Poon, Langmuir **28**, 4618 (2012).

[24] F. Giavazzi, S. Crotti, A. Speciale, F. Serra, G. Zanchetta, V. Trappe, M. Buscaglia, T. Bellini, and R. Cerbino, Soft Matter **10**, 3938 (2014).

[25] L. G. Wilson, V. A. Martinez, J. Schwarz-Linek, J. Tailleur, G. Bryant, P. N. Pusey, and W. C. K. Poon, Phys. Rev. Lett. **106**, 018101 (2011).

[26] V. A. Martinez, R. Besseling, O. A. Croze, J. Tailleur, M. Reufer, J. Schwarz-Linek, L. G. Wilson, M. A. Bees, and W. C. K. Poon, Biophys. J. **103**, 1637 (2012).
[27] M. Reufer, R. Besseling, J. Schwarz-Linek, V. A. Martinez, A. N. Morozov, J. Arlt, D. Trubitsyn, F. B. Ward, and W. C. K. Poon, Biophys. J. **106**, 37 (2014).
[28] K. He, F. Babaye Khorasani, S. T. Retterer, D. K. Thomas, J. C. Conrad, and R. Krishnamoorti, ACS Nano **7**, 5122 (2013).
[29] J. D. C. Jacob, K. He, S. T. Retterer, R. Krishnamoorti, and J. C. Conrad, Soft Matter **11**, 7515 (2015).
[30] Y. Georgalis, P. Umbach, W. Saenger, B. Ihmels, and D. M. Soumpasis, J. Am. Chem. Soc. **121**, 1627 (1999).
[31] W. Pan, O. Galkin, L. Filobelo, R. L. Nagel, and P. G. Vekilov, Biophys. J. **92**, 267 (2007).
[32] K. M. Knee and I. Mukerji, Biochemistry **48**, 9903 (2009).
[33] W. Pan, P. G. Vekilov, and V. Lubchenko, J. Phys. Chem. B **114**, 7620 (2010).
[34] Y. Li, V. Lubchenko, M. A. Vorontsova, L. Filobelo, and P. G. Vekilov, J. Phys. Chem. B **116**, 10657 (2012).
[35] V. Uzunova, W. Pan, V. Lubchenko, and P. G. Vekilov, Faraday Discuss. **159**, 87 (2012).
[36] P. G. Vekilov and M. A. Vorontsova, Acta. Crystallogr. F **70**, 271 (2014).
[37] M. A. Vorontsova, D. Maes, and P. G. Vekilov, Faraday Discuss. **179**, 27 (2015).
[38] D. Maes, M. A. Vorontsova, M. A. C. Potenza, T. Sanvito, M. Sleutel, M. Giglio, and P. G. Vekilov, Acta Crystallogr. F **71**, 815 (2015).
[39] V. Uzunova, W. Pan, O. Galkin, and P. G. Vekilov, Biophys. J. **99**, 1976 (2010).
[40] H. Y. Chan, V. Lankevich, P. G. Vekilov, and V. Lubchenko, Biophys. J. **102**, 1934 (2012).
[41] O. Galkin and P. G. Vekilov, J. Mol. Biol. **336**, 43 (2004).
[42] B. J. Frisken, Appl. Opt. **40**, 4087 (2001).
[43] K. S. Schmitz, *Dynamic Light Scattering by Macromolecules* (Academic, New York, 1990).
[44] O. Gliko, W. Pan, P. Katsonis, N. Neumaier, O. Galkin, S. Weinkauf, and P. G. Vekilov, J. Phys. Chem. B **111**, 3106 (2007).
[45] Y. Li, V. Lubchenko, and P. G. Vekilov, Rev. Sci. Instrum. **82**, 053106 (2011).
[46] D. E. Koppel, J. Chem. Phys. **57**, 4814 (1972).
[47] P. D. Ross and A. P. Minton, Biochem. Biophys. Res. Commun. **76**, 971 (1977).
[48] M. Sleutel and A. E. S. Van Drissche, Proc. Natl. Acad. Sci. USA **111**, E546 (2014).
[49] G. Mie, Ann. Phys. (Leipzig) **330**, 377 (1908).
[50] C. F. Bohren and D. R. Huffman, *Absorption and Scattering of Light by Small Particles* (Wiley-Interscience, New York, 2010).
[51] T. Wriedt, in *The Mie Theory*, edited by W. Hergert and T. Wriedt (Springer-Verlag, Berlin, 2012), pp. 53–71.
[52] C. Mätzler, MATLAB functions for Mie scattering and absorption, Universitas Bernensis Report No. 2002-08.
[53] F. Ferri, D. Magatti, D. Pescini, M. A. C. Potenza, and M. Giglio, Phys. Rev. E **70**, 041405 (2004).
[54] W. Pan, V. V. Uzunova, and P. G. Vekilov, Biopolymers **91**, 1108 (2009).
[55] G. Kwon, B. J. Sung, and A. Yethiraj, J. Phys. Chem. B **118**, 8128 (2014).
[56] L. V. Lorenz and H. Valentiner, *Oeuvres Scientifiques de L. Lorenz* (Librairie Lehmann & Stage, Copenhagen, 1898).
[57] F. Croccolo, D. Brogioli, A. Vailati, M. Giglio, and D. S. Cannell, Appl. Opt. **45**, 2166 (2006).
[58] M. Giglio, M. Carpineti, and A. Vailati, Phys. Rev. Lett. **85**, 1416 (2000).
[59] D. Brogioli, A. Vailati, and M. Giglio, Appl. Phys. Lett. **81**, 4109 (2002).